ELSEVIER

Contents lists available at ScienceDirect

Composites Communications

journal homepage: www.elsevier.com/locate/coco





Light-induced Self-Writing of polymer composites: A novel approach to develop core-shell-type structures

Nathaniel Wellington¹, Shreyas Pathreeker¹, Ian D. Hosein³

Department of Biomedical and Chemical Engineering, Syracuse University, Syracuse, NY, 13244, USA

ARTICLE INFO

Keywords:
Polymer–nanoparticle composite
Photopolymerization
Phase–separation
Magnetic nanoparticles
Vertically–aligned pillars
Raman spectroscopy

ABSTRACT

We employ the Light–Induced Self–Writing (LISW) technique to fabricate vertically–aligned polymer composite microstructures with core–shell morphology. Nanoparticle (NP) organization occurs simultaneously with the structure growth, to form a distinct NP-rich 'shell' layer, and 'core' polymer solid. Photopolymerization–driven NP phase–separation was confirmed using in–situ Raman spectroscopy as well as ex–situ morphology analysis with EDS mapping. The microstructure array obtained consists of uniformly spaced, ~250 µm tall 'pillars' that possess exemplary core–shell morphologies. Our results indicate that LISW is a highly attractive materials fabrication technique towards the development of polymer composite structures.

1. Introduction

Nanoparticle-containing polymer composites are a critical class of materials that find extensive use in many important applications [1-10]. The primary driving force behind the advancement of nanoparticle-containing polymer composites is to enhance overall material properties upon addition of nanoparticles to the neat polymer matrix [11-18]. Furthermore, polymer composite materials fabricated in the form of microneedle- and pillar-arrays have proven useful in advanced applications such as synthetic adhesives [19], pressure-sensing [20], fluid and light manipulation [21], among others [22–25]. Lithography and imprinting are two primary fabrication techniques used to develop such structures, but offer little to no control over the spatial distribution of nanoparticles or filler material in the polymer matrix, which is key to engineering materials for specific applications, particularly in polymer-nanoparticle (NP) composites [26-30]. 3D printing is also a rapidly flourishing technique, and has been used to develop vertically aligned structures [31]. However, 3D printing is slow, as it relies on layer-by-layer (lbl) lateral deposition of material, and achieving control over NP phase-morphology in polymer systems at useful length scales is difficult with 3D printing, as it is with lithography.

The light-induced self-writing (LISW) technique has emerged as a promising approach to the fabrication of micro-pillar arrays. This technique entails the irradiation of a photo-reactive resin with arrays of transmitted optical beams. The photocuring-induced rise in refractive

index induces a self–focusing nonlinearity that balances natural beam divergence, enabling divergence–free light propagation in the resin. In turn, the optical beams induce the growth of microscale fibers in the direction of light propagation. The fiber–optic properties of the growing fiber enable light to be transmitted along the fiber's length towards the growing end, thereby sustaining the propagated growth. The ability to 'self–write' polymer composite structures using light opens attractive avenues in the domain of composite micromaterials fabrication, offering not only rich fundamental material dynamics to explore, but also an effective platform for materials development [29,32–37].

Other methods to develop core–shell morphologies at the sub–micron scale have also been reported. Li et al. [38] developed mono-disperse Fe_3O_4 –coated polystyrene (PS) colloidal particles using a chemical modification approach, which resulted in the core–shell particles demonstrating promising electrical, magnetic, and optical properties. The same authors [39] also recently reported the development of Ag–coated Fe_3O_4 –based nanoparticles for the enhanced detection of dyes such as fluorescein. Rong et al. [40], using a chemical grafting approach, developed surface–functionalized, fluorescein dye/dense SiO_2 –coated Fe_3O_4/SiO_2 nanoparticles for highly stable fluorescence applications. Xu et al. [41] also recently reported a wet chemistry seed–mediated approach to develop nanofibrous polyvinyl alcohol (PVA) mats coated with Au–core, Pd–shell nanoparticles and successfully demonstrated that the mats can function as nanoreactor sites for photocatalytic applications. The shell thickness in these studies was

E-mail address: idhosein@syr.edu (I.D. Hosein).

 $^{^{\}star}$ Corresponding author.

¹ Nathaniel Wellington and Shreyas Pathreeker contributed equally to this work.

between approximately 20 nm and 50 nm. While these studies focused primarily on developing functional core-shell particles at the nano or the sub-nanoscale using wet chemistry procedures, other materials in different forms such as powders and fibers have also been reported. Liu et al. [42], inspired by the structure of the foxtail millet crop, developed MoO₃ nanobelt-core, polypyrrole (PP)/polyaniline (PANI)-shell structures for capacitive energy storage applications using successive polymerization of the conducting polymers to nanoengineer the electrodes. Xu et al. [43] developed self-healing, healing agent-epoxy-core, and PAN-shell fibers using coaxial electrospinning. The fibers were deposited together on hot-dip galvanized (HDG) steel substrates wherein the interconnected fiber-like morphology allowed promising self-healing of the material, along with corrosion resistance. Zhang et al. [44] also employed the coaxial electrospinning technique followed by calcination to develop inorganic Ag-core, BaTiO₃-shell fibers, which were then spin cast in PVDF films to enhance the dielectric properties of the material. The ~12 nm thick BaTiO₃ shell assisted in suppressing conduction losses. Micron-sized powders consisting of NiCo-core C-shell particles for magnetic and electrocatalytic applications were synthesized using an electrochemical approach by Yu et al. [45] CO2-derived carbon was co-reduced on NiO/Co₃O₄ pellets, which resulted in NiCo particles uniformly coated with a 70 nm carbon shell. The final material demonstrated high saturation magnetization and promising hydrogen evolution performance.

The above procedures focus on composite organization at the nanoscale, whereas LISW processes materials morphologically at the microscale. The shell layer in most approaches is generated using external agents, whereas LISW is based on generation of shell layers from the expulsion of NPs that are already present in the initial formulation using visible light. This also contrasts our previous work wherein spray coating was essential to deposit NPs on the surface of the structures [34,37]. The fundamental driving force behind developing core–shell structures is typically either chemical [38–41], electrochemical [45], or in some cases, oxidative polymerization [42], whereas LISW relies on the entropic effects of visible light–induced polymerization on the NPs in suspension.

While wet chemistry procedures can offer nanoscale-level control over shell thickness, their scalability is limited owing to the multiple processing steps and reagents involved. LISW is a simple and scalable approach owing to the simplicity of the initial formulations, and because morphology evolution occurs during the processing step. Coaxial electrospinning, while enabling sub-micron structures, does not offer control over the spatial distribution of NPs. LISW, on the other hand, can offer tunable NP distribution in the polymer at the micrometer scale. Electrochemical methods are suitable for conducting materials such as alloys, but the dielectric nature of polymers and their thermal compatibility with molten electrolytes can be limiting factors. On the other hand, LISW can be used to synthesize C-coated alloy and metal particles owing to the ability of polymers to be carbonized [46,47]. This versatility is an advantage over electrochemical methods, provided the shell thickness and carbon quality are adequately controllable. LISW is also faster due to the rapid and simultaneous vertical growth of structures. The drawbacks associated with incumbent techniques therefore warrants exploration of new methods that offer better control over composite morphology at the microscale.

We recently demonstrated NP phase–separation with SiNPs and photoinitiated acrylate media during LISW [48], and then with TiO₂ NPs for self–cleaning applications [49]. Given the promising nature of pillar–like polymer composite structures, we report here on the use of LISW to form vertically–aligned polymer composite structures with a core–shell–type morphology now using magnetic Fe₃O₄ nanoparticles. Fe₃O₄ nanoparticles offer excellent magnetic functionality and are suitable choices for programmable actuation [21] and soft robotics applications [24], especially when incorporated into array–type polymer structures. There are two key advancements of this work over our previous efforts – 1) the ability to develop arrays of nanoparticle–containing, high aspect

ratio polymer pillar composite structures, and importantly, 2) the ability to simultaneously evolve a core-shell morphology, with a NP shell spatially distributed during the growth process.

2. Experimental section

2.1. Materials

Trimethylolpropane triacrylate (TMPTA) monomer and visible–light photoinitiator camphorquinone (CQ) were purchased from Sigma–Aldrich, USA. PVP–functionalized ${\rm Fe_3O_4}$ nanoparticles with average diameter of 20 nm were purchased from US Research Nanomaterials. All chemicals were used as received.

2.2. Preparation of photopolymerizable mixtures

Photocurable mixtures were prepared by first dissolving the photo-initiator CQ (2.5 wt% of total mixture) in TMPTA (92.5 wt%) monomer. Fe $_3$ O $_4$ nanoparticles (5 wt%) were then dispersed into the mixtures. The mixtures were then continuously stirred overnight in a dark room to protect them from ambient light exposure.

2.3. Photopolymerization of mixtures

The photoreactive mixture was poured into a cell consisting of a Teflon ring adhered to a transparent plastic substrate. The film was irradiated from below with collimated blue light from a light emitting diode (LED) ($\lambda_{max}=470$ nm, Thorlabs Inc.) at an exposure intensity of 2.5 mW/cm². The irradiation time was either 30 or 60 min. After irradiation, the excess monomer was washed away with ethanol, and the sample dried under air flow. Fig. 1 depicts the photopolymerization setup. In the irradiation process, LED light was first passed through a photomask (Photosciences Inc.) consisting of a square array of 40 µm circular apertures spaced 200 µm apart from one another, which generates an optical profile consisting of cylindrical optical beams that are transmitted through the film. The optical pattern consists of bright and dark regions as indicated in Section 2.4, Fig. 1.

2.4. Materials characterization

In–situ Raman spectroscopy was carried out on a Renishaw inVia confocal microscope using methods described previously [35,48]. As shown in Fig. 1, the Raman laser beam was projected from above into a single polymerizing channel (indicated as Bright Region in Section 2.4,

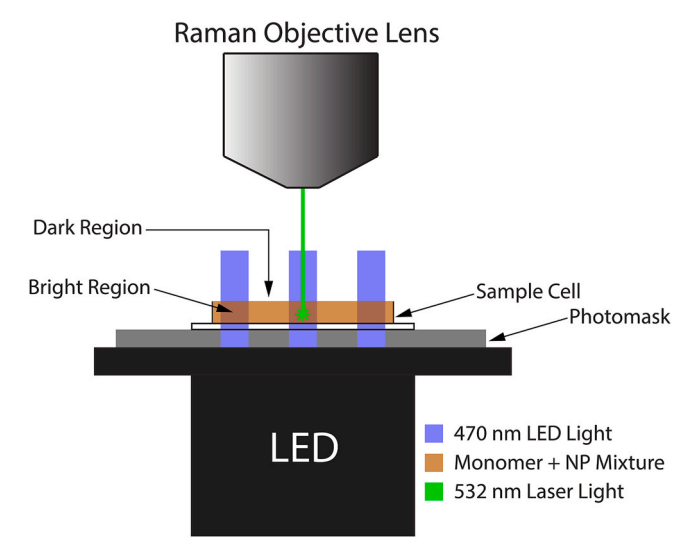


Fig. 1. Schematic of the Raman spectroscopy setup used for in-situ studies.

Fig. 1). The laser spot size was 1.6 μ m, and scans were collected at the inlet face of incident light over 5-min intervals for 60 min, which was the total duration of exposure. Scanning electron microscopy (SEM) was carried out on a JEOL JSM–IT100LA instrument, at an acceleration voltage of 10 or 20 keV. Energy dispersive x–ray spectroscopy (EDS) was carried out on the same instrument at 20 keV. Samples were sputter—coated with gold prior to imaging. Mechanical testing of a representative sample was assessed by placing a standard US dime on the tips of the pillars, which was captured by a digital camera and software (MicroView).

3. Results and discussion

Visible light-induced photopolymerization offers several advantages: the ability to use inexpensive incoherent light sources such as LEDs, which eliminates undesired heat generation, requires less energy to operate, and poses no exposure safety risk compared to other forms of radiation curing like UV curing. Furthermore, tunable photoreactive formulations can be used, and rapid materials fabrication can be obtained. TMPTA monomer was chosen due to its ability to offer fast reaction kinetics owing to its trifunctional nature, and success in previous studies [35,48].

3.1. Structure formation

Fig. 2 shows perspective–view SEM micrographs of polymer composite pillars obtained after exposure times of a), b) 30 min, and c), d) 60 min. Two exposure times were chosen to investigate the attainment of a steady–steady state, both in terms of structure height, and NP migration. Insets in b) and d) show magnified views of the tips of individual pillars. The pillar spacing and base width obtained are exact replicas of the photomask used, i.e. the pillars are $\sim\!40~\mu m$ in diameter and are spaced 200 μm apart, indicating successful transfer of the photomask pattern (spacing and width wise) to the composite photopolymer mixture. Average heights of the 'self–written' polymer composite pillars were 243 μm after 30 min of exposure, and 276 μm after 60 min of exposure, which corresponded to aspect ratios of 5.4:1 and 6:1, respectively. Taller pillars are expected after 60 min of exposure than 30 min of exposure owing to the extended curing. Overall, the

pillars were distributed uniformly and nearly consistent in features. The base diameter D_B of every pillar appears to be greater than its tip diameter D_T , i. e. the pillars are tapered instead of truly cylindrical, which can be attributed to strong photopolymerization at the center of the optical beam relative to its surroundings, and shrinkage of structure diameter closer to the exit face. Notably, there also appears to be a 'necking point' or 'waist' for each pillar between its base and its tip, indicated in Fig. 2b) and d) by white arrows, which is likely formed owing to strong focusing and consequent divergence of the optical beam. Analysis of the higher magnification images (Fig. 2b) and d)) and their insets reveals that the tips of the pillars possess rough, striation–like surfaces, which contrasts with their smooth bases. These striations are likely formed due to lower self–focusing of the optical beam relative to the base–region.

It is also possible to tailor the pillar structure using LISW, as we have shown previously. Pillar height is typically varied by varying the curing time (shorter pillars at shorter curing times), but also by varying the initial film thickness or light intensity [34,50]. Pillar diameter can be varied via the photomask pattern (i.e., dimension of the circular apertures) [34,50].

3.2. Nanoparticle Phase-Separation

Fig. 3 shows the time-lapse in-situ Raman spectroscopy data over exposure time. Monomer Raman intensity was tracked using the peak centered at 1731 cm⁻¹ (C=O moiety) due to its efficacy in determining conversion kinetics [35,48], whereas nanoparticle Raman intensity was tracked using the peak at 678 cm⁻¹.

It can be seen in Fig. 3a) that TMPTA conversion increases over exposure time reaching a maximum of \sim 48% after 55 min of exposure, consistent with previous reports [35,48]. Importantly, Fig. 3b) shows a concurrent decrease in NP Raman intensity over the same exposure time and increase in monomer conversion.

This behavior can be explained as follows. During the irradiation of a two–component photoreactive system (i. e. monomer and nanoparticle mixture), two competing processes occur simultaneously: 1) the photopolymerization reaction which leads to increase in medium viscosity due to polymer chain growth, and 2) the thermodynamic tendency of NPs in the mixture to phase–separate. Photopolymerization kinetics can

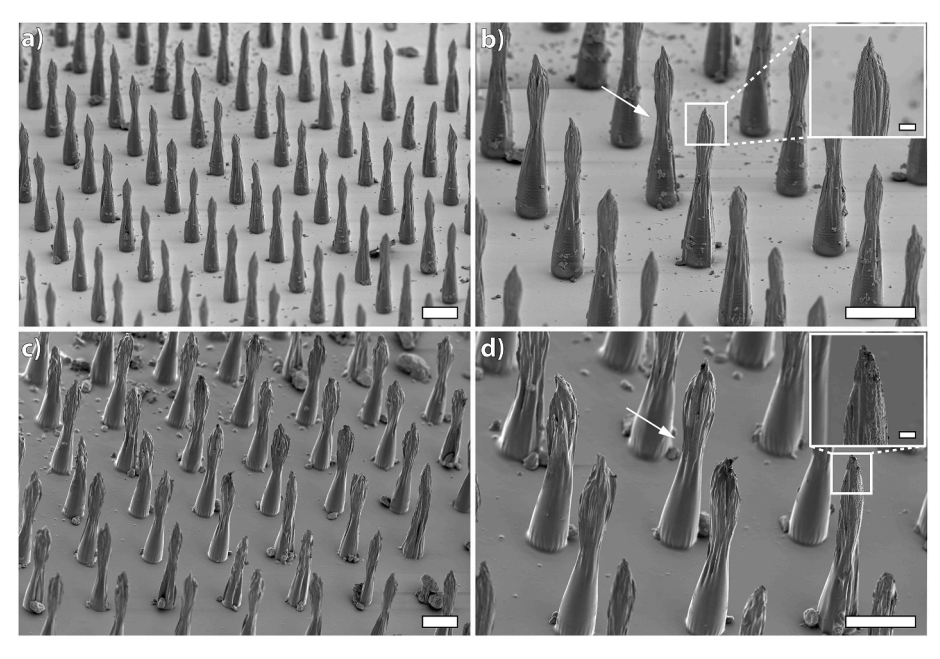
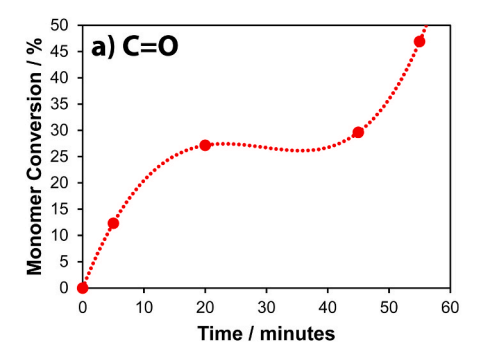


Fig. 2. Perspective–view SEM micrographs of vertically aligned polymer composite pillars obtained after exposure times of a), b) 30 min, and c), d) 60 min. Insets in b) and d) show close–up views of the tips of the respective individual pillars. White arrows indicate the 'necking–point' or 'waist' of the pillars. Scale bars in a)–d) are $100 \mu m$, and those in the insets are $20 \mu m$.



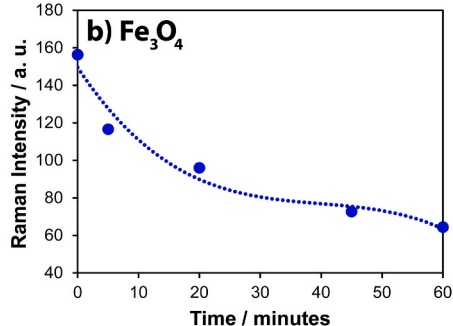


Fig. 3. Representative in–situ Raman scans of a 5 wt% Fe_3O_4 -TMPTA mixture irradiated with a light intensity of 2.5 mW/cm² over 60 min. a) C \equiv O bond conversion of the TMPTA monomer over exposure time, and b) Fe_3O_4 nanoparticle intensity over exposure time.

be controlled by varying incident light intensity, and if the NP radius R_{NP} >> the radius of gyration of the monomer R_g , phase–separation is favored [48,49].

Striking a balance between these two competing processes holds the key to controlling materials morphology during LISW. To facilitate a core–shell morphology, low light intensity was used, and NPs larger (8.5 nm) than the R_g of TMPTA (0.54 nm) [48] were chosen, thereby satisfying the conditions required for NP phase–separation. The simultaneous growth and NP migration mechanism is proposed in the schematic shown in *Fig. 4*. The mechanism of NP attachment to the pillar surface is as follows. As photopolymerization proceeds, the growing polymer chains and the NPs both compete for free volume within the irradiated regions (indicated as Bright Region, *Fig. 1*, Dark Orange Region, *Fig. 4*).

To minimize their free energy within these polymerizing regions, the polymer chains expel the NPs outwards. To minimize their own free energy, the NPs then migrate towards monomer-rich regions (Dark Region, Fig. 1, Light Orange Region, Fig. 4), simply owing to the greater miscibility possible in these lower MW regions. Moreover, the gradient of viscosity between the irradiated (high viscosity) and non-irradiated (low viscosity) regions creates a net flux of NPs between the two regions. As the NPs diffuse outward into the low viscosity regions, their motion is eventually arrested in the highly viscous polymerizing fluid, which lies at the interface between the bright and dark regions, i.e. the TMPTA surface and the uncured monomer. As such, the NPs become embedded in the sub-surface of the photocured structures, thereby generating the 'shell'-type morphology. Therefore, strictly, the NPs are expected to be positioned at the pillar sub-surface rather than on the surface. Nonetheless, a portion of the NPs forms a clear and distinguishable coating on the cured TMPTA pillars. We note that this NP migration process occurs simultaneously with the vertical growth of the pillars owing to light propagation across the film (indicated by the blue arrows in Fig. 4), which is a highlight of the LISW process.

This simultaneous NP migration out of the polymerizing channel driven by the photopolymerization reaction leads to the formation of a NP-coated 'shell' layer, with an NP-depleted polymer 'core' region, giving rise to pillars with core-shell morphologies. Therefore, the concurrent decrease in NP Raman intensity with increase in monomer conversion (as shown in Fig. 3b) confirms photopolymerization induced phase-separation (PhIPS). Furthermore, this process of structure growth and NP phase-separation occurs across the entire propagation length of the optical beams through the film (see schematic in Fig. 4), thereby resulting in the pillar-like structures shown in Section 3.1. Notably, although monomer conversion continues to increase from ~30% after 30 min of exposure to ~48% after 55 min of exposure, the NP Raman intensity appears to plateau within this exposure period (see Fig. 3), indicating that the majority of NP migration occurs within the first 30 min. Hence, the pillar-growth process and the NP phase-separation occur simultaneously.

3.3. Ex-situ morphology analysis using EDS

Fig. 5 shows top-down SEM micrographs and corresponding EDS maps for samples obtained after a), b) 30 min of exposure, and c), d) 60 min of exposure. Insets of Fig. 5a) and b) show cross-sections of individual pillars taken in top-down view and perspective-view, respectively, whereas insets of Fig. 5b) and d) show their corresponding EDS maps for Fe, which is representative of spatial locations of Fe₃O₄ NPs. In the SEM images, cross-sections of the structures appear to be of different sizes, which is an artefact of handling the sample using a razor blade to remove the tips and reveal the core regions of the pillars. The differences in size are owing to the tapered nature of the pillars (base diameter D_B > tip diameter D_T) as discussed in Section 3.1 based on the perspective view SEM images. Based on the perspective-view SEM analysis and top-down SEM images shown here, larger cross-sections represent cross-sections close to the bottom of the pillars, whereas smaller cross--sections represent those close to the tip of the pillars. This difference in sizes aids the morphology analysis in this work, i.e., EDS maps capture cross-sections across a range of different heights, thereby providing crucial information regarding the efficacy of NP phase-separation across pillar height. Dark regions in the EDS maps represent the core regions (NP-deficient), whereas the bright regions represent the shell, i. e. the NPs.

Importantly, the core-shell morphology is observed for all pillars for both exposure times explored (Fig. 5b) and d)), indicating successful NP phase-separation towards the outer surface of the pillars. Inset of Fig. 5d) reveals conformal NP coating of the surface of a representative pillar, further confirming that the NPs are anchored to the outer surface of the structures. The core-shell morphology is preserved across the entire z-axis of the pillars as seen in the EDS maps (i. e. the entire height of the structures shown in Section 3.1). Corresponding insets demonstrate more clearly this core-shell morphology associated with a representative pillar, indicated by dashed circles, wherein the NP shell size appears to be \sim 5 μm . The extent of NP coating on the surface can be controlled by finely controlling the NP movement during photopolymerization via incident light-intensity. NP-core, polymer-shell structures, can also be obtained by trapping the NPs can be within the rapidly polymerizing structure using a sufficiently high irradiation intensity [48]. An area of continued study is on tuning NP-monomer interactions to achieve more control over NP positioning. These results corroborate the in-situ Raman spectroscopy data shown in Fig. 3. The EDS maps do not indicate significant differences in morphology between the two exposure times explored here, confirming that 30 min is sufficient to facilitate phase-separation of NPs.

Lastly, because enhanced mechanical properties are a signature of polymer composite materials, we assessed the mechanical robustness of a representative sample in a simple manner. A standard US dime weighing 2.268 g was placed horizontally on the tips of polymer composite pillars obtained after 30 min of curing. We found that despite possessing an aspect ratio of 5.4:1, the polymer composite pillars were

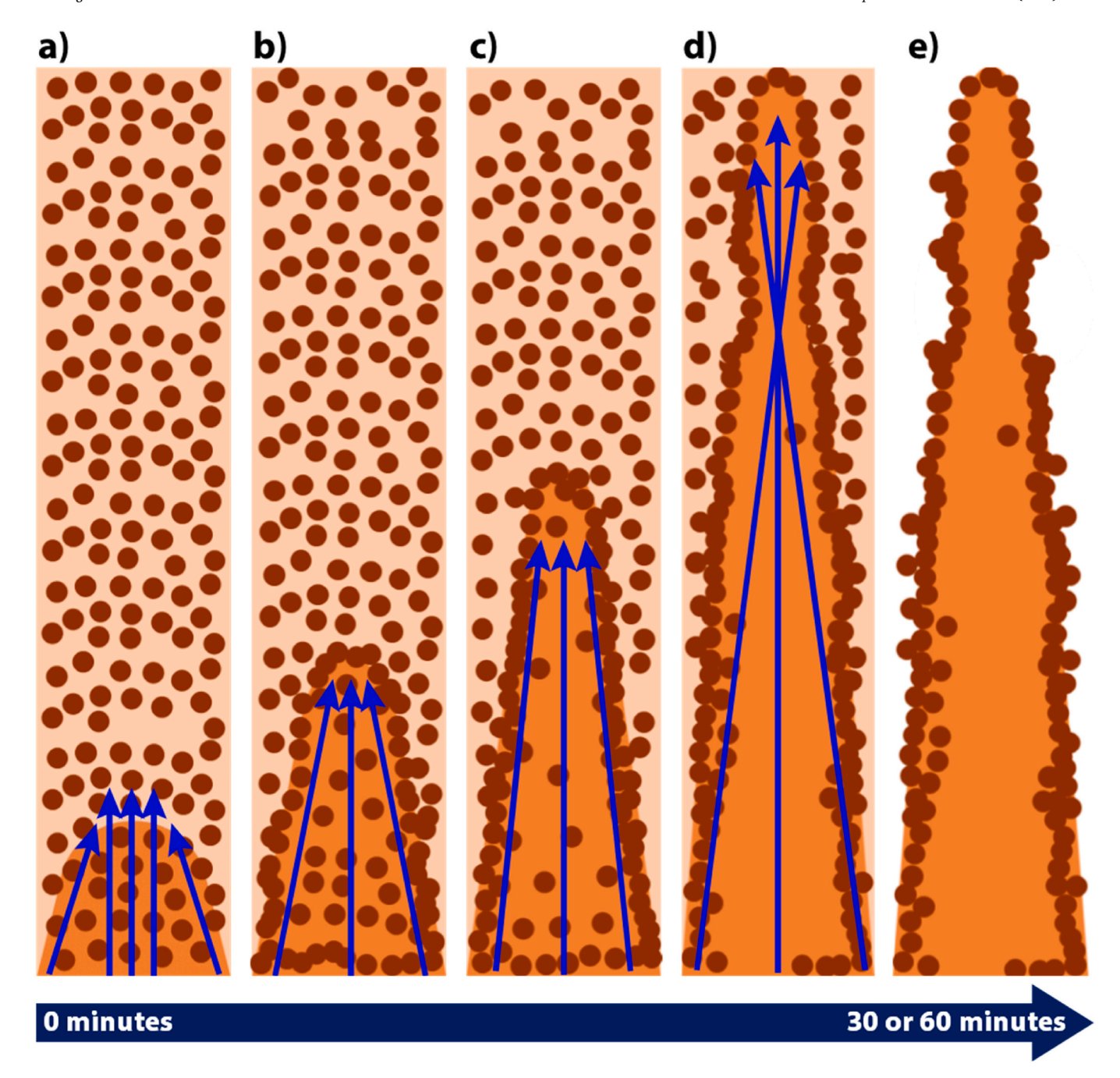


Fig. 4. Proposed mechanism of the concurrent growth and NP migration process versus exposure time: a) Initiation of LISW using visible blue light, b) Photopolymerization—induced pillar growth and simultaneous NP expulsion towards low viscosity monomer regions, c) Continued pillar growth and formation of NP–shell, d) Optical refocusing and trapping of NPs at sub–surface of cured pillars, and e) Final polymer–core, NP–shell structures after 30 or 60 min. Blue arrows represent the incident blue light, light orange is low viscosity monomer, dark orange is highly viscous, cured polymer, and brown is Fe₃O₄ NPs. (For interpretation of the references to colour in this figure legend, the reader is referred to the Web version of this article.)

able to support the coin without collapsing, indicating their practically useful mechanically robust nature.

4. Conclusion

In conclusion, fabrication of vertically–aligned polymer-Fe $_3$ O $_4$ -NP composite pillars has been demonstrated in this work using the Light–Induced Self–Writing (LISW) technique, based on visible light–induced photopolymerization. Tall composite structures on the order of $\sim\!250$ μm were obtained in a simple processing step, and these structures were found to possess exemplary core–shell morphology owing to concurrent

NP migration during pillar growth. The LISW technique provides an excellent platform for developing polymer composite structures in a simple and straightforward manner.

Further work should be focused on 1) developing mesoscale structures with high NP weight loading to impart sufficient functionality to the material, 2) more finely tuning the NP position during photopolymerization, 3) exploring different NP-monomer systems to obtain sophisticated materials with more advanced functionalities, and 4) Systematically assessing the properties of such structures for magnetic and optical applications, which are both active areas of our continued investigations.

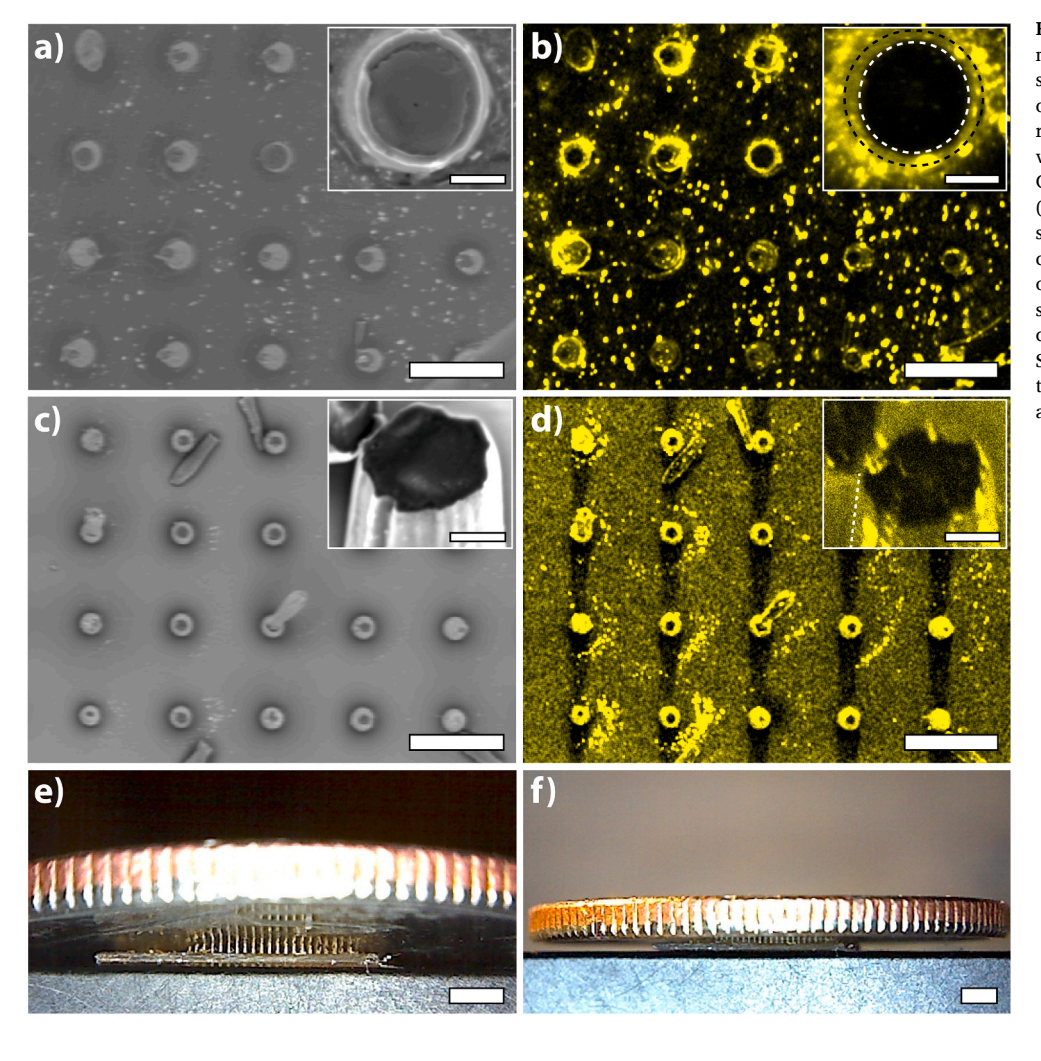


Fig. 5. Top-down view backscatter SEM micrographs of pillars obtained after exposure times of a) 30 min, and c) 60 min. Insets of a) and c) show cross-sections of the respective individual pillars in top-down view and perspective-view, respectively. Corresponding EDS maps are shown in b) (30 min), and d) (60 min), with insets showing the corresponding individual cross-sections. Macrolens images of an array of polymer composite pillars supporting a standard US dime weighing 2.268 g in e) close-up view, and f) in zoomed-out view. Scale bars in a)-d) are 200 µm, and those in the insets are 20 µm, whereas scale bars in e) and f) are approximately 5 mm.

CRediT authorship contribution statement

Nathaniel Wellington: Investigation, Visualization, Formal analysis, and . Shreyas Pathreeker: Visualization, Formal analysis, Writing – original draft, Writing – review & editing, contributed equally to this work. Ian D. Hosein: Conceptualization, Supervision, Project administration, Funding acquisition, Writing – review & editing.

Declaration of competing interest

The authors declare that they have no known competing financial interests or personal relationships that could have appeared to influence the work reported in this paper.

Acknowledgements

The authors gratefully acknowledge financial support from the National Science Foundation (NSF) under CAREER award number CMMI–1751621. The authors also acknowledge financial support from the 3M Foundation (NTFA), and the College of Engineering and Computer Science at Syracuse University, NY.

References

[1] E. Bet-moushoul, Y. Mansourpanah, K. Farhadi, M. Tabatabaei, TiO2 nanocomposite based polymeric membranes: a review on performance improvement for various applications in chemical engineering processes, Chem. Eng. J. 283 (2016) 29–46.

- [2] M. Dziadek, E. Stodolak-Zych, K. Cholewa-Kowalska, Biodegradable ceramicpolymer composites for biomedical applications: a review, Mater. Sci. Eng. C 71 (2017) 1175–1191.
- [3] R. Elhajjar, C.-T. Law, A. Pegoretti, Magnetostrictive polymer composites: recent advances in materials, structures and properties, Prog. Mater. Sci. 97 (2018) 204–229
- [4] H. Abbasi, M. Antunes, J.I. Velasco, Recent advances in carbon-based polymer nanocomposites for electromagnetic interference shielding, Prog. Mater. Sci. 103 (2019) 319–373.
- [5] D. Nepal, W.J. Kennedy, R. Pachter, R.A. Vaia, Toward architected nanocomposites: MXenes and beyond, ACS Nano 15 (2021) 21–28.
- [6] C.Z. Liang, T.-S. Chung, J.-Y. Lai, A review of polymeric composite membranes for gas separation and energy production, Prog. Polym. Sci. 97 (2019) 101141.
- [7] M. Kalaj, K.C. Bentz, S. Ayala, J.M. Palomba, K.S. Barcus, Y. Katayama, et al., MOF-polymer hybrid materials: from simple composites to tailored architectures, Chem. Rev. 120 (2020) 8267–8302.
- [8] R. Poupart, D. Grande, B. Carbonnier, B. Le Droumaguet, Porous polymers and metallic nanoparticles: a hybrid wedding as a robust method toward efficient supported catalytic systems, Prog. Polym. Sci. 96 (2019) 21–42.
- [9] F. Ye, K. Liao, R. Ran, Z. Shao, Recent advances in filler engineering of polymer electrolytes for solid-state Li-ion batteries: a review, Energy Fuel. 34 (2020) 9189–9207
- [10] S. Tajik, H. Beitollahi, F.G. Nejad, Z. Dourandish, M.A. Khalilzadeh, H.W. Jang, et al., Recent developments in polymer nanocomposite-based electrochemical sensors for detecting environmental pollutants, Ind. Eng. Chem. Res. 60 (2021) 1112–1136.
- [11] G. Schmidt, M.M. Malwitz, Properties of polymer–nanoparticle composites, Curr. Opin. Colloid Interface Sci. 8 (2003) 103–108.
- [12] C. Balazs Anna, T. Emrick, P. Russell Thomas, Nanoparticle polymer composites: where two small worlds meet, Science 314 (2006) 1107–1110.
- [13] M.J.A. Hore, R.J. Composto, Functional polymer nanocomposites enhanced by nanorods, Macromolecules 47 (2014) 875–887.
- [14] S.K. Kumar, B.C. Benicewicz, R.A. Vaia, Winey KI. 50th anniversary perspective: are polymer nanocomposites practical for applications? Macromolecules 50 (2017) 714–731.

- [15] H. Emamy, S.K. Kumar, F.W. Starr, Diminishing interfacial effects with decreasing nanoparticle size in polymer-nanoparticle composites, Phys. Rev. Lett. 121 (2018) 207801
- [16] E.J. Bailey, K.I. Winey, Dynamics of polymer segments, polymer chains, and nanoparticles in polymer nanocomposite melts: a review, Prog. Polym. Sci. 105 (2020) 101242.
- [17] H. Emamy, S.K. Kumar, F.W. Starr, Structural properties of bound layer in polymer–nanoparticle composites, Macromolecules 53 (2020) 7845–7850.
- [18] Z. Zhang, J. Du, J. Li, X. Huang, T. Kang, C. Zhang, et al., Polymer nanocomposites with aligned two-dimensional materials, Prog. Polym. Sci. 114 (2021) 101360.
- [19] D.-J. Guo, R. Liu, Y. Cheng, H. Zhang, L.-M. Zhou, S.-M. Fang, et al., Reverse adhesion of a gecko-inspired synthetic adhesive switched by an ion-exchange polymer-metal composite actuator, ACS Appl. Mater. Interfaces 7 (2015) 5409.
- [20] H. Park, Y.R. Jeong, J. Yun, S.Y. Hong, S. Jin, S.-J. Lee, et al., Stretchable array of highly sensitive pressure sensors consisting of polyaniline nanofibers and Aucoated polydimethylsiloxane micropillars, ACS Nano 9 (2015) 9974–9985.
- [21] Z. Yang, J.K. Park, S. Kim, Magnetically responsive elastomer-silicon hybrid surfaces for fluid and light manipulation, Small 14 (2018) 1702839.
- [22] G. Tullii, F. Giona, F. Lodola, S. Bonfadini, C. Bossio, S. Varo, et al., High-aspect-ratio semiconducting polymer pillars for 3D cell cultures, ACS Appl. Mater. Interfaces 11 (2019) 28125–28137.
- [23] H. Kang, H. Lai, Z. Cheng, Y. Liu, L. Jiang, Restoration of superwetting switching on TiO2 coated shape memory polymer arrays, Chem. Eng. J. 394 (2020) 124996.
- [24] Z. Wang, K. Wang, D. Liang, L. Yan, K. Ni, H. Huang, et al., Hybrid magnetic micropillar arrays for programmable actuation, Adv. Mater. 32 (2020) 2001879.
- [25] Salwa, N.T. Chevala, S.R. Jitta, S.M. Marques, V.M. Vaz, L. Kumar, Polymeric microneedles for transdermal delivery of nanoparticles: frontiers of formulation, sterility and stability aspects, J. Drug Deliv. Sci. Technol. 65 (2021) 102711.
- [26] R.A. Vaia, J.F. Maguire, Polymer nanocomposites with prescribed morphology: going beyond nanoparticle-filled polymers, Chem. Mater. 19 (2007) 2736–2751.
- [27] X. Yang, J. Loos, Toward high-performance polymer solar cells:the importance of morphology control, Macromolecules 40 (2007) 1353–1362.
- [28] D.W. Shin, M.D. Guiver, Y.M. Lee, Hydrocarbon-based polymer electrolyte membranes: importance of morphology on ion transport and membrane stability, Chem. Rev. 117 (2017) 4759–4805.
- [29] I.D. Hosein, Light-directed organization of polymer materials from photoreactive formulations, Chem. Mater. 32 (2020) 2673–2687.
- [30] T. Bian, R. Klajn, Morphology Control in Crystalline Nanoparticle-Polymer Aggregates, Annals of the New York Academy of Sciences, 2021 n/a.
- [31] C. Chen, B. Ran, Z. Wang, H. Zhao, M. Lan, H. Chen, et al., Development of micropillar array electrodes for highly sensitive detection of biomarkers, RSC Adv. 10 (2020) 41110–41119.
- [32] F.-H. Chen, S. Biria, H. Li, I.D. Hosein, Microfiber optic arrays as top coatings for front-contact solar cells toward mitigation of shading loss, ACS Appl. Mater. Interfaces 11 (2019) 47422–47427.
- [33] S. Biria, F.-H. Chen, I.D. Hosein, Enhanced wide-angle energy conversion using structure-tunable waveguide arrays as encapsulation materials for silicon solar cells. Phys. Status Solidi 216 (2019) 1800716.
- [34] H. Li, F.H. Chen, S. Biria, I.D. Hosein, Prototyping of superhydrophobic surfaces from structure-tunable micropillar arrays using visible light photocuring, Adv. Eng. Mater. 21 (2019) 1801150.

- [35] S. Biria, I.D. Hosein, Control of morphology in polymer blends through light self-trapping: an in situ study of structure evolution, reaction kinetics, and phase separation, Macromolecules 50 (2017) 3617–3626.
- [36] S. Biria, F.H. Chen, S. Pathreeker, I.D. Hosein, Polymer encapsulants incorporating light-guiding architectures to increase optical energy conversion in solar cells, Adv. Mater. 30 (2018) 1705382.
- [37] S. Biria, I.D. Hosein, Superhydrophobic microporous substrates via photocuring: coupling optical pattern formation to phase separation for process-tunable pore architectures, ACS Appl. Mater. Interfaces 10 (2018) 3094–3105.
- [38] Y. Li, W. Duan, A. Fujisaka, T. Moriga, X. Lu, S. Yang, A facile two-step approach to synthesize monodisperse and high-magnetization Fe304@ PS composite colloidal particles for constructing dual-response photonic crystals, Comp. Commun. 19 (2020) 114–120.
- [39] Y. Li, W. Duan, Highly significant fluorescence enhancement effect of silver-deposited Fe3O4@ C core/shell nanoparticles for detection of dyes and fluorescein, Comp. Commun. 28 (2021) 100964.
- [40] H. Rong, T. Gao, X. Zhang, Improved fluorescence stability for Fe3O4/silica@ fluorescein/dense silica structure with double shell, Comp. Commun. 20 (2020) 100368
- [41] L. Xu, X. Wang, T. Ma, X. Zhao, Seed-mediated growth of Au core–Pd shell-structured nanoparticles on a polymer nanofibrous mat as a highly active photocatalytic composite material, Comp. Commun. 21 (2020) 100406.
- [42] Y. Liu, L. Li, J. Zhu, J. Xu, S. Liu, Y. Wang, et al., A biomimetic Setaria viridisinspired electrode with polyaniline nanowire arrays aligned on MoO 3@ polypyrrole core-shell nanobelts, J. Mater. Chem. 6 (2018) 13428–13437.
- [43] S. Xu, J. Li, H. Qiu, Y. Xue, J. Yang, Repeated self-healing of composite coatings with core-shell fibres, Comp. Commun. 19 (2020) 220–225.
- [44] Y-s Zhang, M. Wang, C. Yang, Y-w Shao, X-d Qi, J-h Yang, et al., Heterogeneous BaTiO3@ Ag core-shell fibers as fillers for polymer dielectric composites with simultaneously improved dielectric constant and breakdown strength, Comp. Commun. 27 (2021) 100874.
- [45] R. Yu, B. Deng, K. Zheng, X. Wang, K. Du, D. Wang, A facile strategy to synthesize graphitic carbon-encapsulated core-shell nanocomposites derived from CO2 as functional materials, Comp. Commun. 22 (2020) 100464.
- [46] A. Berenbaum, M. Ginzburg-Margau, N. Coombs, A.J. Lough, A. Safa-Sefat, J. E. Greedan, et al., Ceramics containing magnetic Co-Fe alloy nanoparticles from the pyrolysis of a highly metallized organometallic polymer precursor, Adv. Mater. 15 (2003) 51–55.
- [47] G.-L. Wen, H.-J. Niu, J.-J. Feng, X. Luo, X. Weng, A.-J. Wang, Well-dispersed Co3Fe7 alloy nanoparticles wrapped in N-doped defect-rich carbon nanosheets as a highly efficient and methanol-resistant catalyst for oxygen-reduction reaction, J. Colloid Interface Sci. 569 (2020) 277–285.
- [48] S. Pathreeker, F.-H. Chen, S. Biria, I.D. Hosein, Observation of intensity dependent phase-separation in photoreactive monomer—nanoparticle formulations under nonuniform visible light irradiation. Soft Matter 16 (2020) 7256–7269.
- [49] S. Pathreeker, P. Chando, F.-H. Chen, S. Biria, H. Li, E.B. Finkelstein, et al., Superhydrophobic polymer composite surfaces developed via photopolymerization, ACS Appl. Polym. Mater. 3 (2021) 4661–4672.
- [50] F.H. Chen, S. Pathreeker, S. Biria, I.D. Hosein, Synthesis of micropillar arrays via photopolymerization: an in situ study of light-induced formation, growth kinetics, and the influence of oxygen inhibition, Macromolecules 50 (2017) 5767–5778.